

Lidar calibration and validation for geometric-optical modeling with Landsat imagery

Authors:

Gang Chen ^a, Michael A. Wulder ^{a,*}, Joanne C. White ^a, Thomas Hilker ^b, and Nicholas C. Coops ^c

Affiliations:

^a *Canadian Forest Service (Pacific Forestry Centre), Natural Resources Canada, 506 West Burnside Road, Victoria, British Columbia, V8Z 1M5, Canada*

^b *Biospheric Sciences Branch, NASA Goddard Space Flight Center, 8800 Greenbelt Road, Greenbelt, Maryland, 20771, USA*

^c *Integrated Remote Sensing Studio, Department of Forest Resources Management, Faculty of Forestry, University of British Columbia, 2424 Main Mall, Vancouver, British Columbia, V6T 1Z4, Canada*

* Corresponding author: Mike Wulder. E-mail address: mwulder@nrcan.gc.ca

Pre-print of published version.

Reference:

Chen, G., M.A. Wulder, J.C. White, T.H. Hilker, and N.C. Coops. (2012). Lidar calibration and validation for geometric-optical modeling with Landsat. *Remote Sensing of Environment*. (Accepted May 30, 2012).

DOI.

<http://dx.doi.org/10.1016/j.rse.2012.05.026>

Disclaimer:

The PDF document is a copy of the final version of this manuscript that was subsequently accepted by the journal for publication. The paper has been through peer review, but it has not been subject to any additional copy-editing or journal specific formatting (so will look different from the final version of record, which may be accessed following the DOI above depending on your access situation).

1 **Abstract**

2 There is a paucity of detailed and timely forest inventory information available for
3 Canada's large, remote northern boreal forests. The Canadian National Forest Inventory
4 program has derived a limited set of attributes from a Landsat-based land cover product
5 representing circa year 2000 conditions. Of the required inventory attributes, forest
6 vertical structure (e.g., tree height) is critical for terrestrial biomass and carbon modeling
7 and to date, is unavailable for these remote areas. In this study, we develop a large-area,
8 fine-scale (25 m) mapping solution to estimate tree height (mean, dominant, and Lorey's
9 height) across Canada's northern forests by integrating lidar data (representing 0.27% of
10 the study area), and Landsat imagery (representing 100% of the study area), using a
11 geometric-optical modeling technique. First, spectral mixture analysis (SMA) was used to
12 extract image endmembers and generate fraction images. Second, lidar data were used to
13 calibrate the inverted geometric-optical model by adjusting the model's three key
14 fractional inputs: sunlit crown, sunlit background, and shade fraction, based upon the
15 SMA derived images. The heterogeneity of the study area, spanning 2.16 million ha,
16 made it challenging to directly and accurately decompose mixed Landsat image pixels
17 into the canopy and background fractions used for the Li-Strahler geometric-optical
18 model inversion. As a result we developed a novel method to use the lidar plot data to
19 facilitate the calculation of these fractions in an accurate and automated manner. The
20 average estimation errors for mean, dominant, and Lorey's height were 4.9 m, 4.1 m, and
21 4.7 m, respectively when compared to the lidar data, with the best result achieved using
22 dominant tree height, where the average error was 3.5 m for over 80% of the forested
23 area. Using this approach of optical remotely sensed data calibrated and validated with
24 lidar height estimates we generate and evaluate wall-to-wall estimates of tree height that
25 can subsequently be used as inputs for biomass and carbon modeling.

26
27 *Keywords:* Tree height; Landsat; Lidar plots; Li-Strahler geometric-optical model; Large-
28 area

29 **1. Introduction**

30 Boreal forests are one of world's largest biomes, responsible for approximately 22% of
31 terrestrial carbon stored in the global forests (Pan et al., 2011). Compared to tropical
32 forests, the boreal forests contain almost twice the amount of carbon per unit area
33 (Potapov et al., 2011), most of which is contained in soil organic matter. Forest
34 management and reporting activities require accurate, timely, and consistent information
35 which typically supports forest inventories. However, much of the boreal forest
36 ecosystem occurs at high latitudes (45° to 65°) (Brandt, 2009) where human access is
37 limited and industrial forest management is typically not practiced due to low forest
38 productivity, small trees, and long distances to markets (Wulder et al., 2007). While there
39 is some elasticity to the managed forest area constraints such as fuel costs, presence of
40 road networks, and timber values, climate and productivity remain the limiting factors in
41 these northern forests and the subarctic and cold continental climate is a major
42 impediment to human activities in this biome (Potapov et al., 2008). Outside of the
43 southern boreal where industrial activities are practiced, natural ecosystem processes tend
44 to dominate the northern portions of the Canadian boreal forest (Andrew et al., 2012),
45 with low populations and few roads (Wulder et al., 2007). As such, forest inventory in the
46 northern boreal is logistically challenging, labor intensive, and expensive. For example,
47 Andersen et al. (2009) reported an average cost of \$6,000 USD to establish one ground
48 plot on the Kenai Peninsula of Alaska. Similar costs have been found in Canada, based on
49 plot installation activities for the National Forest Inventory (NFI). As a result, an alternate
50 means of collecting data and characterizing forest conditions is highly desired.

51 The boreal forests of Canada extend from Newfoundland across Canada into
52 Alaska, with its northern extent generally considered to be at the southern limit of the
53 tundra, and its southern extent coincident with the northern limit of temperate forests
54 (recognizing variations at both extremes according to local topography, climate, and
55 edaphic conditions) (Brandt, 2009). Much of British Columbia is considered hemi-boreal,
56 and other areas excluded from the boreal include eastern Maritime forests, central
57 Canadian mixed woods, and the agricultural zones of the west. To date, large areas of
58 Canada's boreal forests lack detailed and timely forest inventory information as they are
59 not monitored by provincial or territorial resource management agencies. In these areas,
60 Canada's federal NFI program has relied on a Landsat-based land cover product
61 generated by the Earth Observation for Sustainable Developments of forests (EOSD)
62 project, representing circa 2000 conditions, to provide relevant information for this
63 northern portion of the Canadian boreal (Gillis et al., 2005; Wulder et al., 2008b). While
64 current protocols have integrated very high spatial resolution satellite data as a surrogate
65 for aerial photography in the north (Falkowski et al., 2009; Mora et al., 2010), additional
66 information is required to provide spatially explicit forest structural information.

67 Forest vertical structural information is critical for forest monitoring and
68 inventory. While optical imagery has been shown to be able to effectively capture forest
69 area (Haapanen et al., 2004), cover types (Wulder et al., 2008b), and change in area
70 (Stehman, 2009), knowledge of forest presence/absence is only part of the information
71 required by monitoring and inventory programs. Forest vertical structure provides
72 information on "how much", to complement the more readily produced "where is"
73 information. Knowledge of tree height, for instance, provides information on volume,
74 biomass, and—in conjunction with modeling—age. As such, forest vertical structure

75 (especially tree height) is a critical NFI attribute. Tree height is known to correlate
76 strongly with the biomass and carbon in forest ecosystems (Flanagan and Johnsen, 1995;
77 Lefsky et al., 2002; Ni-Meister et al., 2010). Although the term “tree height” is used,
78 apart from dedicated single tree applications (e.g., Gougeon and Leckie, 2006; Forzieri et
79 al., 2009), it is typically an areal generalization of height that is generated, either stand
80 height portrayed within an inventory polygon, or an average height attributed to a
81 particular image pixel. In this research (as typical elsewhere) we refer to tree height as
82 related to the areal generalization of height over a pixel. Further, from an inventory
83 perspective, stand height is defined as the height of the leading species (i.e., the species
84 with the greatest proportion of basal area in the stand) in the tallest horizontal stratum in
85 the stand, with the goal of capturing the characteristics of the larger trees in a stand,
86 indicative of the merchantable volume present. Pixel based approaches typically do not
87 partition height by strata.

88 In recent years, lidar (light detection and ranging) technology flown on airborne
89 platforms has become increasingly standardized and established for measuring forest
90 vertical structure with a high degree of accuracy (Lim et al., 2003; Zhao et al., 2011),
91 with notable relevance to forest management (Wulder et al., 2008a). Compared to field
92 mensuration, lidar provides a relatively cost-efficient solution to estimate tree height;
93 however, wall-to-wall airborne lidar surveys over large areas remain expensive (Chen
94 and Hay, 2011a). In terms of accuracy, Næsset and Okland (2002) found multiple lidar
95 measures of the same trees to have less variance than from multiple, manual, field
96 measures. To reduce data acquisition costs whilst collecting useful estimates of forest
97 vertical structure, recent efforts have focused on the development of integrated models
98 using samples of lidar data to represent large areas (for a review, see Wulder et al., 2012),
99 often using wall-to-wall optical remotely sensed data to create strata to support the spatial
100 extension of estimates (e.g., Boudreau et al., 2008). Successful applications of lidar to
101 sample and represent a population require sufficient sampling density and appropriate
102 placement of samples, among other issues. However, the accuracy of lidar measures for
103 predicting forest structure offers unique opportunities to also consider using the lidar
104 attributes (calibrated against ground data) as calibration and validation data in empirical
105 approaches to generate structural attributes from optical imagery. Further, a sample
106 density that is too sparse for robust population level estimates may be sufficiently large
107 and have value in conferring local structural conditions.

108 Following on the ideas above, lidar data can be viewed as providing plot-like
109 information, enabling model calibration and validation. As such, models can be
110 developed to spatially extend lidar-measured attributes over larger extents using image
111 analysis. This type of approach has been applied by others with the research divided into
112 two groups: those that apply parametric approaches (Chen et al., 2011; Hilker et al.,
113 2008; Hudak et al., 2002; Hyde et al., 2006; Wulder and Seemann, 2003), and those that
114 do not (Chen et al., 2012; McInerney et al., 2010; Stojanova et al., 2010). A typical
115 parametric approach uses multiple regression which defines relationships between image
116 spectral metrics and lidar-measured tree height. Although widely used and easy to
117 interpret, this empirical approach often lacks the ability to characterize forest complexity,
118 especially at fine spatial scales (Chen and Hay, 2011b), and most of these approaches
119 were undertaken at the stand level, where internal stand forest structural variability has
120 been reduced (Wulder and Seemann, 2003; Hilker et al., 2008). Alternatively, non-

121 parametric machine learning techniques, such as support vector machines, have
122 demonstrated superior performances over classic regression analysis for estimating tree
123 height (Chen and Hay, 2011b; Zhao et al., 2011). However, most of these tools, as used
124 in remote sensing studies of forests, have a black-box nature that can prohibit users from
125 defining (or understanding) the relationship between model inputs and outputs.

126 While the integration of lidar and optical data through these parametric and non-
127 parametric approaches to generating and extending forest vertical attributes over large
128 areas has been well established, geometric-optical (GO) approaches provide an
129 alternative which has proved useful for estimation of vegetation biophysical parameters
130 (Chen et al., 2000; Chopping et al., 2006; Franklin and Turner, 1992; Liang, 2007; Peddle
131 et al., 2003; Zeng et al., 2008) from canopy reflectance. The advantage of a geometric-
132 optical (hereafter, GO model) approach over aforementioned approaches is that these
133 kinds of models are typically based on physical principles of the geometric structures of
134 discontinuous canopies which, in theory, allow these approaches to be used in a more
135 generic fashion and across ecosystems. As the most widely used GO model, the Li-
136 Strahler model estimates the fractions of four forest components (sunlit canopy, sunlit
137 background, shaded canopy, and shaded background) as a function of tree size (e.g.,
138 height, crown dimensions) and tree density (Li and Strahler, 1985; 1992). The premise of
139 the approach is that, if the fractions of these components (sunlit and shaded crown and
140 background) can be accurately extracted from the remotely sensed imagery, it is possible
141 to predict tree height through inversion of the model.

142 Implementation of the Li-Strahler model in a northern boreal environment
143 presents unique considerations. First, northern boreal forest stands are distributed on less
144 productive sites with relatively low tree densities, resulting in background components
145 that typically exhibit high spectral heterogeneity, as they are typically characterized by
146 bare soils and/or low vegetation. This heterogeneity causes difficulties in the accurate
147 extraction of the four forest fractions used for GO models. Second, there are typically few
148 field plots available in these areas, confounding model calibration and validation. Third,
149 previous studies have found that the Li-Strahler model gives more reliable estimates of
150 forest cover than height, and that the non-linearity of the model inversion process may
151 introduce errors into height estimates (Woodcock et al., 1994; 1997); however, these
152 studies were limited by the amount of data available for independent calibration. Lidar
153 data provides a potential means to address these issues, by providing a large number of
154 detailed forest structural measurements with which to calibrate the inverted Li-Strahler
155 GO model by adjusting the input fractions, thereby enabling a more accurate estimation
156 of tree height.

157 The primary objective of this study is therefore to develop a large-area, fine-scale
158 (25 m) mapping approach for estimation of tree height in the Canada's northern forest
159 environment. To do so, we propose to integrate sample of airborne lidar plots and
160 Landsat data, within the Li-Strahler GO model. Here, lidar plots refer to a defined,
161 spatially discrete areas similar in size to a ground plot from which tree characteristics
162 (i.e., tree height, crown dimensions), as well as metrics generalizing the plot-wide vertical
163 structural conditions, are extracted from lidar data.

165 **2. Materials**

166 *2.1. Study area*

167 While the focus of our study is the northern boreal we develop and demonstrate the
168 approach at a study site in western Manitoba (centered at: 55°54'N, 99°30'W), Canada,
169 covering an area of approximately 2.16 million ha (Fig. 1). As a typical region in the
170 Boreal Shield, the largest of Canada's ecozones (Environment Canada, 2000), the area is
171 characterized by forest, wetlands, and lakes, with wildfire the dominant agent of
172 disturbance (Stocks et al., 2003). The forest is dominated by conifers, including black
173 spruce (*Picea mariana*), white spruce (*Picea glauca*), balsam fir (*Abies balsamea*), jack
174 pine (*Pinus banksiana*), as well as a small proportion of deciduous trees, such as paper
175 birch (*Betula papyrifera*), trembling aspen (*Populus tremuloides*), and balsam poplar
176 (*Populus balsamifera*). Mean annual temperatures range between -15°C in January and
177 17°C in July, and mean annual precipitation is around 400 mm (Environment Canada,
178 2000). Topographically, the site has an average elevation of 273 m above sea level,
179 ranging from 45 m to 494 m with a mean slope of 4°.

180 [INSERT FIG. 1]

181

182 2.2. Lidar plots

183 Lidar data were collected from a national-scale forest lidar acquisition campaign
184 performed during the summer of 2010, when a series of 34 individual transects with a
185 total length of more than 24,000 km were flown across eight ecozones and 13 Universal
186 Transverse Mercator (UTM) zones of Canada. A segment of one lidar transect
187 (approximately 145 km long) was used to acquire forest structure variability for the study
188 site (Fig. 1). Lidar data were acquired using a discrete return lidar system (Optech ALTM
189 3100). The survey specifications included a flying height of 1,200 m above ground level,
190 a pulse repetition frequency of 70 kHz, scan angles of +/-15°, and a nominal pulse density
191 of ~3 returns/m². Following the data acquisition, lidar metrics (e.g., percentile values) and
192 CHM (canopy height model) were calculated for 625 m² (25-by-25 m) plots that fell
193 within the approximately 400 m lidar swath using FUSION (McGaughey, 2000). Only
194 non-ground returns greater than 2 m in height were used for metric calculation. There
195 were 92,800 25-by-25 m lidar plots representing approximately 0.27% of the study area.

196 With plot-level lidar metrics (e.g., percentile values) and field data, Bater et al.
197 (2011) developed multiple linear regression models to estimate three plot-level height
198 attributes: mean height, dominant height, and Lorey's height, resulting in low RMSEs
199 (root mean square errors) of approximately 1.5 m. Mean height is calculated as the
200 arithmetic mean height of all trees in the plot, and dominant height is calculated as the
201 arithmetic mean height of the four tallest trees in the plot. Lorey's height is calculated by
202 multiplying, for each tree in the plot, the tree height by its basal area, then summing these
203 values and dividing the total by the total basal area of the plot. Each of these height
204 measures has importance to forest inventory and management, hence our interest in their
205 estimation.

206 After excluding non-treed areas from the sample, 81,045 lidar plots remained for
207 use as reference data. Summary statistics for these plots are provided in Table 1. We
208 extracted 10% of the lidar plots for calibration, and another 10% from the remainder for
209 validation. We used a stratified random selection strategy (Husch et al., 2002), where the
210 10% samples were taken from each 1.0 m height interval from the minimum to the
211 maximum height. Compared to a simple random sampling, this method considered all
212 tree height strata, ensuring a more reasonable representation of the population. Fig. 2

213 shows a comparison of three dominant tree height histograms derived from all lidar data,
214 and the selected calibration and validation data. All three histograms are highly correlated
215 with each other ($R>0.95$).

216 [INSERT TABLE 1]

217 [INSERT FIG. 2]

218

219 2.3. Landsat imagery

220 A Landsat-5 Thematic Mapper (TM) scene (Path 34, Row 21) of the study site was
221 acquired on June 5, 2010 from the USGS archive in L1T format (orthorectored). The
222 cloud-free area of the image was used to determine the extent of the study area.
223 Compared to low spatial resolution (i.e., 250/500/1000 m MODIS) and high spatial
224 resolution optical satellites (e.g., 0.6/2.4 m QuickBird), Landsat (30 m) provides an
225 appropriate resolution for balancing the need to collect fine-scale forest information with
226 the requirements for reducing data acquisition and processing costs for large-area forest
227 inventory and management. Compared to satellites with similar resolutions (e.g., 23 m
228 IRS), Landsat offers free and open access to data (Wulder et al., 2011). In this study,
229 Landsat bands 1-5 and 7 were converted to at-sensor radiances, which were then
230 converted to top-of-atmosphere (TOA) reflectance (Chander et al., 2009). To facilitate
231 the comparison between Landsat imagery and lidar plots, the Landsat scene was
232 resampled from the original 30 m to 25 m (consistent with the lidar plot size) using the
233 nearest neighbor method. The image was acquired with the solar zenith angle of 35.5° and
234 a solar azimuth angle of 152.9° .

235

236 2.4. ASTER elevation data

237 The elevation data utilized in this study was collected by ASTER (Advanced Spaceborne
238 Thermal Emission and Reflection Radiometer) as part of the GDEM (Global Digital
239 Elevation Model) project (version 1). The accuracy of GDEM version 1 at the 95%
240 confidence level is 21.31 m (RMSE 10.87 m) (ASTER GDEM Validation Team, 2009),
241 although a lower error is expected in our study area due to the flat topography with a
242 mean slope of 4.02 degrees. The DEM (30 m resolution) was resampled to the resolution
243 of 25 m using the nearest neighbor method to be consistent with the resolution of Landsat
244 image and the size of lidar plots. Aspect and slope images were also generated to
245 represent the study area.

246

247 3. Methods

248 In this section, we first summarize the overall methodological flow, with dedicated
249 subsections below providing required detail. Forested areas within the study site were
250 delineated using a supervised classification of the Landsat imagery. Tree height
251 information from lidar plots was used to aid in the collection of training data, by
252 distinguishing various ground features, such as trees from non-treed low vegetation. We
253 then calculated the forest fractional components (sunlit crown, sunlit background and
254 shade fractions), which are critical inputs of the inverted Li-Strahler GO model. This was
255 completed by using spectral mixture analysis (SMA) and lidar plots. To do so, the first
256 step was to collect spectral endmembers, the reflectance spectra of the 'pure' pixels
257 (Keshava and Mustard, 2002). This was followed by the calculation of fraction images,
258 corresponding to the abundance of all endmembers. However, due to the high spectral

259 variability resulting from the aforementioned heterogeneity of these forests, these SMA
260 fractions may not accurately represent the inputs of the inverted Li-Strahler model. For
261 example, two or more SMA endmembers may correspond to the same fractional
262 component (e.g., a sunlit background may be represented by exposed soils, low
263 vegetation, or the mixture thereof). Tree heights derived from lidar plots were used to
264 calibrate the inverted Li-Strahler GO model by tuning the three fractional components,
265 with results validated by independent lidar plots. The flowchart in Fig. 3 summarizes
266 these steps; while the following sub-sections provide greater detail and explanation.

267 [INSERT FIG. 3]

268

269 3.1. Forest extraction

270 In this study, we applied a supervised maximum likelihood classification algorithm
271 (Richards, 1999) to Landsat multispectral bands 3, 4, 5, and 7 to generate four major
272 classes: forest, water, exposed land, and low vegetation (including shrubs, herbs and
273 bryoids), as per Canada's EOSD circa 2000 land cover product (Wulder et al., 2008b). To
274 reduce the impact of haze present when the image was acquired, bands 1 and 2 were
275 excluded from our analysis (Chavez, 1988). Training data for each of the classes were
276 selected manually. The forest and low vegetation classes were difficult to distinguish due
277 to their spectral similarity and the lack of field measurements. To address this issue, we
278 used a 1 m CHM derived from the lidar data to guide the selection of appropriate training
279 samples by verifying the structure differences between trees and low vegetation (Fig. 4).

280 [INSERT FIG. 4]

281

282 3.2. Fraction calculation

283 Spectral mixture analysis (SMA) is one of the most popular techniques used to address
284 the spectral heterogeneity present in remote sensing pixels, and it has been widely used in
285 forestry applications (e.g., Peddle et al., 1999; Zeng et al., 2008). SMA estimates the
286 proportions of pure components within each mixed pixel, which typically contains more
287 than one ground cover type (Somers et al., 2011). In this study, SMA was applied to
288 generate sub-pixel fraction images for the pixels in the forest class (as identified in the
289 previous section).

290 One prerequisite to successful pixel unmixing using SMA is the selection of
291 representative endmembers (Somers et al., 2011; Tompkins et al., 1997). In this study,
292 endmembers were derived from the Landsat multispectral image (bands 3, 4, 5 and 7),
293 rather than a spectral library, enabling ease of association with image features (Franke et
294 al., 2009; Rashed et al., 2003). In this study, endmembers were selected using the
295 Sequential Maximum Angle Convex Cone (SMACC) algorithm, which finds extreme
296 vectors (i.e., endmembers) that cannot be represented by a positive linear combination of
297 other vectors (Gruninger et al., 2004), similar to principal components analysis. A key
298 benefit of the SMACC algorithm is that it is fast, has no requirement of *a priori*
299 knowledge of the study area, and exhibits reliable performance, which is desirable for
300 large-area applications. The number of endmembers was determined based on two
301 criteria: (i) the SMACC relative error tolerance was 0.01, and (ii) the SMACC relative
302 error began to converge markedly when additional endmembers were used. Fig. 5 shows
303 a relative error plot, where five endmembers were finally selected, as the addition of
304 more endmembers only marginally increased the SMACC performance, although greatly

305 increasing the computational expense. The corresponding fraction (i.e., abundance)
306 images were simultaneously generated based upon the assumption that the spectrum of a
307 mixed pixel is a linear combination of the endmember spectra weighted by their area
308 fractions, and the fractions of each pixel are constrained to sum to one (Gruninger et al.,
309 2004):

$$310 \quad H_{i,j} = \sum_n^N S_{i,n} F_{n,j}^N + R_{i,j}^N \quad (1)$$

311 Where, $H_{i,j}$ is the reflectance in the i -th channel of the j -th pixel, n is the endmember
312 indices from 1 to the expansion length N , S is a matrix that contains the endmember
313 spectra, F is a matrix that contains the fractional contribution (between 0 and 1) of each
314 basis endmember spectrum to each pixel, and R is an error term.

315 [INSERT FIG. 5]

316

317 3.3. Geometric-optical model inversion

318 The Li-Strahler GO model simulates the complex relationship between sunlit and shaded
319 canopy and background, and tree density and canopy geometric structure (h – the height
320 from the ground to mid-crown, b – the half crown height, and r – the half crown width)
321 (Li and Strahler, 1992). In the forward mode, the inputs are tree density and canopy
322 geometric structure, producing outputs of the fractions of the four image components. By
323 inverting the model, the data inputs and outputs are switched and we are able to predict
324 canopy vertical structure (e.g., tree height: $h+b$) from the four fractions. Typically, shaded
325 canopy and shaded background fractions are grouped for assessing forest canopy
326 structure under an assumption that both components have the same reflectance (Peddle et
327 al., 1999). It is therefore critical to obtain accurate fractions of the three components of
328 sunlit canopy, sunlit background, and shade.

329 While unsupervised SMA methods such as SMACC are more practical to apply over
330 large areas, one of the disadvantages is that the endmembers are not assigned to one of
331 the three inputs of the inverted Li-Strahler model. Additionally, more SMA derived
332 endmembers may represent the same GO model required image component. For example,
333 the two types of backgrounds covered by bare soils and low vegetation have distinct
334 reflectance, possibly leading to the definition of two endmembers. This issue can
335 potentially be mitigated by using lidar-measured tree height to calibrate the inverted Li-
336 Strahler model by tuning the model's input fractions. In this study, tree height was
337 estimated in the following four main steps:

338 (1) We assigned the SMACC generated five endmembers to the three image components
339 (i.e., sunlit crown, sunlit background and shade). Consequently, the corresponding five
340 SMACC fraction images were combined to simulate the three inputs of the inverted Li-
341 Strahler model. Since SMACC is an unsupervised method, it remains unclear which
342 endmember should belong to which image component. To solve this issue, we evaluated
343 all the possible assignment combinations—a total number of 150.

344 (2) For each assignment combination, we performed the Li-Strahler model inversion
345 using the combined fractions, topographic data (aspect and slope images), and solar and
346 viewing angles. Mathematically, the inversion of the Li-Strahler model is a non-linear
347 minimization problem that can be solved through iterative adjustment of estimated a-
348 priori inputs (Verstraete et al., 1996). The inversion problem can be defined as the
349 minimum of a cost function C :

350
$$C = \sqrt{\sum_{i=1}^n [F_i(R) - F_i(T)]^2} \quad (2)$$

351 where, $F(R)$ are the fractions extracted from the spectral reflectance (i.e., combined SMA
 352 fractions), $F(T)$ represents the fractions calculated using the Li-Strahler model in forward
 353 mode with tree structure parameters (including tree height) as inputs, and n is the number
 354 of pixels. Different optimization algorithms are available; in this study, we selected a
 355 trust-region-reflective algorithm based on the interior-reflective Newton method to
 356 determine the “best” tree height (Coleman and Li, 1996; Coleman et al., 2002). Lidar
 357 measured tree structure information was also used to constrain the algorithm and avoid
 358 unrealistic results. For example, the lidar measured tree heights (Table 1) were used as *a*
 359 *priori* knowledge to force the model inversion to generate height estimates within the
 360 same range.

361 (3) The tree height estimates from all the possible fraction combinations were evaluated
 362 using lidar training plots, where the “best” combination was considered to result in the
 363 lowest average estimation error for height.

364 (4) The corresponding estimated tree heights were further validated using independently
 365 selected lidar validation plots.

366 The use of lidar plots provided an accurate way for calibrating the inverted Li-
 367 Strahler model through an automatic adjustment of the three fractional inputs. As
 368 indicated in section 2.2, the lidar calibration data included estimates of mean height,
 369 dominant height, and Lorey’s height for each lidar plot. These three different measures of
 370 tree height were estimated individually from the GO model by running the process
 371 described above three times.

372

373 **4. Results and Discussion**

374 *4.1. Endmember spectra and fraction images*

375 In Fig. 6 we present the spectral reflectance of the five SMA extracted endmembers (E1,
 376 E2, E3, E4, and E5). By following the methods in Section 3.3, we found the best
 377 combination of these fraction images: sunlit crown—(E1), sunlit background—(E2+E3),
 378 and shade— (E4+E5), which were all used for estimating mean height, dominant height,
 379 and Lorey’s height. Fig. 6 shows that the spectra of E1, E4 and E5 have a major
 380 difference in the NIR (near-infrared: 760-900 nm) band, where, as expected, the sunlit
 381 crown has a higher reflectivity contribution than the shade. E4 is different from E5 with a
 382 slightly higher reflectance in the NIR band. One possible reason could be that E5 was
 383 closer to the ground and it was therefore mixed with a higher percentage of low
 384 vegetation (e.g., shrub and grass) and/or soils, which typically have a higher water
 385 content than tree leaves, enabling a stronger absorption of NIR. Compared to the sunlit
 386 crown and shade endmembers, it is more apparent that E2 and E3 belong to the sunlit
 387 background, especially in the shortwave-infrared (band 5, SWIR-1: 1550-1750 nm and
 388 band 7, SWIR-2: 2080-2350 nm) bands, as they have higher spectral reflectance than
 389 those from trees and shade. The difference between E2 and E3 may be due to the
 390 distinctions in soil properties (e.g., moisture content).

391
$$[INSERT FIG. 6]$$

392

393 The fraction images (of the full study site) corresponding to the three components
 394 of sunlit crown, sunlit background, and shade are shown in Fig. 7. Sparse forest stands

395 tended to have lower sunlit crown and shade fractions due to the lack of trees than dense
396 forest stands, while the sunlit background fractions are higher. A typical example of the
397 sparse forests in Fig. 7 is a large patch close to the center of the study area. For a viewing
398 of the site, please refer to Fig. 1, where the patch is in light green tone representing a
399 group of forest stands regenerating after wildfire. Fig. 7 illustrates that the findings from
400 these fraction images are consistent with the assumption, as the regenerated forest stands
401 have low sunlit crown and shade fractions and are dominated by a large portion of sunlit
402 backgrounds.

403 [INSERT FIG. 7]

404

405 4.2. Tree height

406 Fig. 8 presents both the estimation errors (grey bars) and the area percentages (lines) of
407 different tree height classes for (a) mean height, (b) dominant height, and (c) Lorey's
408 height. The height classes (with 3-m interval) are: HT1 (2-5 m), HT2 (5-8 m), HT3 (8-11
409 m), HT4 (11-14 m), HT5 (14-17 m), HT6 (17-20 m), HT7 (20-23 m), HT8 (13-27 m),
410 and HT9 (27-30 m). The 3-m interval was selected to aid in the interpretation of the
411 estimation errors. The average estimation errors (i.e., RMSEs) are 4.9 m, 4.1 and 4.7 m
412 for each of mean, dominant, and Lorey's height, respectively. The best model
413 performance (i.e., lowest RMSE) was achieved for dominant tree height, which could be
414 caused by two factors: (i) the signals received by Landsat were biased to the upper level
415 of forest canopies; and (ii) the dominant trees have a greater likelihood of intercepting the
416 laser pulses as noted by Popescu et al. (2002). Model performance for Lorey's height,
417 which is mean tree height weighted by the basal areas of all trees, was better than for
418 simply averaged mean height and worse than for dominant height.

419 [INSERT FIG. 8]

420

421 Errors were not uniform across all height classes. In particular, relatively small
422 (i.e., HT1-2) and tall trees (HT7-9) have errors of over 6.0 m for all the three height
423 measures (Fig. 8). A potential reason could be that small trees are typically located within
424 sparse forest stands and the background in these stands is a major contributor to the
425 spectral reflectance. Additionally, forest background is rarely only covered by bare soils,
426 but rather is often a mixture of soils and low vegetation. The heterogeneous background
427 tends to exhibit strong reflectance anisotropy, causing difficulties for the Li-Strahler GO
428 model to estimate tree height with nadir data (Chopping et al., 2006; Gemmell, 2000).
429 For tall trees, which are often mature, the sunlit crown tends to show a darker tone than
430 other trees. This may have introduced errors in the fraction extraction using SMA.
431 However, we noted that these five height classes accounted for only a small portion of the
432 site, i.e., 2.9%, 15.4% and 8.1% for mean height, dominant height, and Lorey's height.
433 The majority of the trees (over 80% by area) in the forested area ranged from 8 to 20 m
434 (classes HT3-6), where the tree vertical structure was reasonably well estimated (Fig. 8).
435 Especially for the three classes of HT4, HT5 and HT6, the height estimation errors were
436 between 2.1 m and 3.9 m. In the case of estimating dominant tree height, the mean error
437 was 3.5 m for 81.2% of the forested area, which shows comparable performance with
438 other studies in the similar forest environment at the stand level. For example, Wulder
439 and Seemann (2003) reported a height estimation error of 3.3 m using Landsat imagery to
440 estimate lidar-measured canopy height in Saskatchewan, Canada. The average stand size

441 used in their study was 14.2 ha. Similarly, Hilker et al. (2008) updated forest inventory
442 attributes using high-spatial-resolution QuickBird imagery and a lidar transect in British
443 Columbia, Canada. Their height prediction resulted in an error of 3.5 m using inventory
444 polygons, which were typically larger than 2.0 ha in that area. More recently, Chen et al.,
445 (2012) applied similar data types of QuickBird imagery and lidar transects to estimate
446 tree height in a Quebec study site. By incorporating machine learning techniques, they
447 obtained an error of 3.4 m at the plot level of 0.04 ha. Compared to the estimates at the
448 large forest stand level, height variability in our study was better retained using small
449 plots (25-by-25 m), with the wall-to-wall estimates of tree height presented in Fig. 9.
450 Wildfire boundaries have been overlaid on the height output to aid in illustrating the
451 capacity of the wall-to-wall estimates to inform on stand vertical structure. Inset A in Fig.
452 9 shows an undisturbed forest and wetland area, where tree heights (right) typically
453 increase with increasing distance from wetland features (as seen in the RGB Landsat
454 image using a composite of bands 5, 4 and 3 on the left; shorter trees are clustered around
455 wetland features). Inset B illustrates an area that was burned by wildfire in 1995. Outside
456 the area of the fire, the natural variation in vertical structure as a function of site and
457 topography is observed. Inside the fire perimeter, the spatial variability in fire impacts are
458 evident, where areas of moderately tall trees that were not consumed by fire remain,
459 along with areas of regenerating forests. Fig. 9 indicates that the height estimates from
460 this study can be further linked with other landscape ecology research (e.g., wetlands and
461 wildfire) as an important environmental variable.

462 [INSERT FIG. 9]

463

464 Given the results of previous research by Woodcock et al. (1994 and 1997) we
465 had modest expectations for the capacity of a GO model driven approach to estimate tree
466 heights, as these previous studies indicate that the GO model's estimates of forest cover
467 are more reliable than its estimates of tree size. The iterative approach we have applied in
468 this current research, using a large sample of plot-like data (from the lidar) to calibrate,
469 validate, and re-calibrate as required, may have enabled the improved estimates of height
470 achieved in this study. Furthermore, of the studies indicated above [e.g., Hilker et al.
471 (2008) and Chen et al. (2012)], the prediction errors on height estimates are lower (i.e.,
472 3.5 m and 3.4 m) than those reported herein, but these studies used high spatial resolution
473 imagery. While difficult to compare across studies (e.g., the spatial precision of the
474 estimates will differ), it is worth noting that the mapping effort per unit area is less for
475 Landsat with the larger imaging footprint (185 × 185 km) in contrast to the high spatial
476 resolution imagery, with typical extents of 10 × 10 km.

477 The intention is that for areas of Canada where spatially explicit forest inventory
478 information is lacking, image derived estimates could fulfill this information need. For
479 instance, the carbon budget model used by the Government of Canada to represent the
480 forest sector—the Carbon Budget Model of the Canadian Forest Sector (CBM-CFS3)—
481 operates using stand-based inventory data (Natural Resources Canada, 2012). The
482 generation of pixel-based structural attributes corresponding to the required model inputs,
483 generalized using image segmentation to replicate forest stands, may form a basis for
484 using CBM-CFS3 over these remote locations. Currently, Canada meets national and
485 international carbon reporting objectives by focusing on the managed forest using CBM-
486 CFS3. Additional Earth-system science questions that encompass the entire forested area

487 of Canada in a consistent and transparent manner follow the generation of remotely
488 sensed inputs to aid in model parameterization.

489

490 **5. Conclusions**

491 Outside of Canada's managed forest area, such as the more northern forests, there can be
492 a lack of detailed and timely forest inventory information. To reduce data costs while
493 collecting large-area, fine-scale (25 m) grid-based tree height estimates over Canada's
494 northern forests, we have developed a novel mapping solution integrating lidar plots,
495 representing 0.27% of the study area, Landsat imagery, and the Li-Strahler geometric-
496 optical model. As it is challenging to accurately identify the image endmembers required
497 by the Li-Strahler model, lidar data were used to calibrate the three critical model inputs
498 of sunlit crown, sunlit background, and shade fractions. We have evaluated the model
499 performance for estimating three measures of plot-level tree height: mean, dominant, and
500 Lorey's height. Based upon the results of this study, we found that the three forest
501 components (i.e., sunlit crown, sunlit background, and shade) were spectrally
502 heterogeneous. By applying the spectral mixture analysis to the Landsat imagery, we
503 found five endmembers, rather than three, which best represented the conditions present
504 in this boreal study site. The best result (lowest tree height estimation error) shows that
505 these endmembers corresponded to one type of sunlit crown, two types of sunlit
506 backgrounds, and two types of shade. Here, lidar plots were used as calibration data,
507 which helped assign the endmembers to individual forest components in an accurate and
508 automated manner. This also reduces the possibility of introducing errors caused by an
509 inaccurate human interpretation of the endmembers. We also found that the average
510 estimation errors were 4.9 m, 4.1, and 4.7 m for mean height, dominant height, and
511 Lorey's height, respectively. The best result was achieved for characterizing the dominant
512 tree height, where the average error was 3.5 m for 81.2% of the forested area. It should be
513 noted that the non-linear GO model inversion process may have introduced errors, which
514 can be reduced by using more accurate *a priori* knowledge to better constrain tree
515 parameters. The coregistration between lidar data and Landsat image at the pixel level
516 was another likely source of error due to their different data acquisition geometries.
517 Future research will evaluate object-based approaches using polygons as basic units in
518 tree height estimation to reduce this error. However, learning from and augmenting other
519 studies in similar forest environments, our approach presents an advancement towards the
520 characterization of wall-to-wall forest vertical structure over large areas using Landsat
521 imagery and airborne (or perhaps satellite) lidar sample datasets in a time- and cost-
522 efficient manner

523

524 **Acknowledgements**

525 This research has been funded by a Natural Sciences and Engineering Research Council
526 (NSERC) Visiting Fellowship award to Dr. Gang Chen. Aspects of this research were
527 undertaken as part of the "EcoMonitor: Northern Ecosystem Climate Change
528 Monitoring" project jointly funded by the Canadian Space Agency (CSA) Government
529 Related Initiatives Program (GRIP) and the Canadian Forest Service (CFS) of Natural
530 Resources Canada.

531

References

- 532 Andersen, H. E., Barrett, T., Winterberger, K., Strunk, J., & Temesgen, H. (2009).
533 Estimating forest biomass on the western lowlands of the Kenai Peninsula of
534 Alaska using airborne lidar and field plot data in a model-assisted sampling design.
535 In: *Proceedings of Extending forest inventory and monitoring, IUFRO Division 4*,
536 Quebec City, Canada, May 19-22, 5 p.
- 537 Andrew, M.E., Wulder, M.A., & Coops, N.C. (2012). De facto protected areas of the
538 Canadian boreal forest. *Biological Conservation*. DOI:
539 <http://dx.doi.org/10.1016/j.biocon.2011.11.029>.
- 540 ASTER GDEM Validation Team (2009). *ASTER Global DEM Validation: Summary*
541 *Report. June 2009*. Available online (accessed February 24, 2012):
542 [http://www.ersdac.or.jp/GDEM/E/image/ASTERGDEM_ValidationSummaryRepo](http://www.ersdac.or.jp/GDEM/E/image/ASTERGDEM_ValidationSummaryReport_Ver1.pdf)
543 [rt_Ver1.pdf](http://www.ersdac.or.jp/GDEM/E/image/ASTERGDEM_ValidationSummaryReport_Ver1.pdf).
- 544 Bater, C.W., Wulder, M.A., Coops, N.C., Hopkinson, C., Coggins, S.B., Arsenault, E.,
545 Beaudoin, A., Guindon, L., Hall, R.J., Villemaire, P., & Woods, M. (2011). Model
546 development for the estimation of aboveground biomass using a lidar-based sample
547 of Canada's boreal forest. *SilviLaser 2011*, Oct. 16-19, 2011, Hobart, Tasmania,
548 Australia.
- 549 Boudreau, J., Nelson, R. F., Margolis, H. A., & Beaudoin, A. (2008). Regional
550 aboveground forest biomass using airborne and spaceborne LiDAR in Quebec.
551 *Remote Sensing of Environment*, 112, 3876–3890.
- 552 Brandt, J.P. (2009). The extent of the North American boreal zone. *Environmental*
553 *Reviews*, 17, 101–161.
- 554 Chander, G., Markham, B.L., & Helder, D.L. (2009). Summary of current radiometric
555 calibration coefficients for Landsat MSS, TM, ETM+, and EO-1 ALI sensors.
556 *Remote Sensing of Environment*, 113, 893–903.
- 557 Chavez, P.S. (1988). An improved dark-object subtraction technique for atmospheric
558 scattering correction of multispectral data. *Remote Sensing of Environment*, 24,
559 459–479.
- 560 Chen, G., & Hay, G.J. (2011a). An airborne lidar sampling strategy to model forest
561 canopy height from Quickbird imagery and GEOBIA. *Remote Sensing of*
562 *Environment*, 115, 1532–1542.
- 563 Chen, G., & Hay, G.J. (2011b). A support vector regression approach to estimate forest
564 biophysical parameters at the object level using airborne lidar transects and quick
565 bird data. *Photogrammetric Engineering and Remote Sensing*, 77, 733–741.
- 566 Chen, G., Hay, G.J., Castilla, G., St-Onge, B., & Powers, R. (2011). A multiscale
567 geographic object-based image analysis (GEOBIA) to estimate lidar-measured
568 forest canopy height using Quickbird imagery. *International Journal of Geographic*
569 *Information Science*, 25, 877–893.
- 570 Chen, G., Hay, G.J., & St-Onge, B. (2012). A GEOBIA framework to estimate forest
571 parameters from lidar transects, Quickbird imagery and machine learning: A case
572 study in Quebec, Canada. *International Journal of Applied Earth Observations and*
573 *Geoinformation*, 15, 28–37.
- 574 Chen, J. M., Li, X., Nilson, T., & Strahler, A. (2000). Recent advances in geometrical
575 optical modelling and its applications. *Remote Sensing Reviews*, 18, 227–262.

- 576 Chopping, M. J., Su, L., Laliberte, A., Rango, A., Peters, D.P.C., & Kollikkathara, N.
577 (2006). Mapping shrub abundance in desert grasslands using geometric-optical
578 modeling and multi-angle remote sensing with CHRIS/Proba. *Remote Sensing of*
579 *Environment*, 104, 62–73.
- 580 Coleman, T.F., & Li, Y.Y. (1996). An interior trust region approach for nonlinear
581 minimization subject to bounds. *Siam Journal on Optimization*, 6, 418–445.
- 582 Coleman, T.F., Liu, J.G., & Yuan, W. (2002). A new trust-region algorithm for equality
583 constrained optimization. *Computational Optimization and Applications*, 21,
584 177–199.
- 585 Environment Canada (2000). *Ecological Assessment of the Boreal Shield Ecozone*.
586 Available online (accessed February 24, 2012):
587 [http://www.ec.gc.ca/Publications/1F4C0C47-4E18-4988-8514-](http://www.ec.gc.ca/Publications/1F4C0C47-4E18-4988-8514-A842EED6F774%5CEcologicalAssessmentOfTheBorealShieldEcozone.pdf)
588 [A842EED6F774%5CEcologicalAssessmentOfTheBorealShieldEcozone.pdf](http://www.ec.gc.ca/Publications/1F4C0C47-4E18-4988-8514-A842EED6F774%5CEcologicalAssessmentOfTheBorealShieldEcozone.pdf).
- 589 Falkowski, M. J., Wulder, M. A., White, J. C., & Gillis, M. D. (2009). Supporting large-
590 area, sample-based forest inventories with very high spatial resolution satellite
591 imagery. *Progress in Physical Geography*, 33, 403–423.
- 592 Flanagan, L.B., & Johnsen, K.H. (1995). Genetic variation in carbon isotope
593 discrimination and its relationship to growth under field conditions in full-sib
594 families of *Piceamariana*. *Canadian Journal of Forest Research*, 25, 39–47.
- 595 Forzieri, G., Guarnieri, L., Vivoni, E. R., Castelli, F., & Preti, F. (2009). Multiple
596 attribute decision making for individual tree detection using high-resolution laser
597 scanning. *Forest Ecology and Management*, 258, 2501–2510.
- 598 Franke, J., Roberts, D.A., Halligan, K., & Menz, G. (2009). Hierarchical Multiple
599 Endmember Spectral Mixture Analysis (MESMA) of hyperspectral imagery for
600 urban environments. *Remote Sensing of Environment*, 113, 1712–1723.
- 601 Franklin, J., & Turner, D.L. (1992). The application of a geometric optical canopy
602 reflectance model to semiarid shrub vegetation. *IEEE Transactions on Geoscience*
603 *and Remote Sensing*, 30, 293–301.
- 604 Gemmell, F. (2000). Testing the Utility of Multi-angle Spectral Data for Reducing the
605 Effects of Background Spectral Variations in Forest Reflectance Model Inversion.
606 *Remote Sensing of Environment*, 72, 46–63.
- 607 Gillis, M.D., Omule, A.Y., & Brierley, T. (2005). Monitoring Canada’s forests: the
608 National Forest Inventory. *The Forestry Chronicle*, 81, 214–221.
- 609 Gougeon, F. A., & Leckie D. G. (2006). The individual tree crown approach applied to
610 IKONOS images of a coniferous plantation area. *Photogrammetric Engineering*
611 *and Remote Sensing*, 72, 1287–1297.
- 612 Gruninger, J., Ratkowski, A.J., & Hoke, M.L. (2004). The Sequential Maximum Angle
613 Convex Cone (SMACC) endmember model. In *SPIE Proceeding, Algorithms for*
614 *Multispectral and Hyper-spectral and Ultraspectral Imagery*, 5425-1, 122–135.
- 615 Haapanen, R., Ek, A. R., Bauer, M. E., & Finley, A. O. (2004). Delineation of
616 forest/nonforest land use classes using nearest neighbor methods. *Remote Sensing of*
617 *Environment*, 89, 265–271.
- 618 Hilker, T., Wulder, M.A., & Coops, N.C. (2008). Update of forest inventory data with
619 lidar and high spatial resolution satellite imagery. *Canadian Journal of Remote*
620 *Sensing*, 34, 5–12.

- 621 Hudak, A.T., Lefsky, M.A., Cohen, W.B., & Berterreche, M. (2002). Integration of
622 LIDAR and Landsat ETM+ data for estimating and mapping forest canopy height.
623 *Remote Sensing of Environment*, 82, 397–416.
- 624 Hyde, P., Dubayah, P., Walker, W., Blair, J.B., Hofton, M., & Hunsaker, C. (2006).
625 Mapping forest structure for wildlife habitat analysis using multi-sensor (LiDAR,
626 SAR/InSAR, ETM+, Quickbird) synergy. *Remote Sensing of Environment*, 102,
627 26–36.
- 628 Keshava, N., & Mustard, J.F. (2002). Spectral unmixing. *IEEE Signal Processing*
629 *Magazine*, 19, 44–57.
- 630 Lefsky, M. A., Cohen, W. B., Harding, D. J., Parkers, G. G., Acker, S. A., & Gower, S.
631 T. (2002). Lidar remote sensing of above-ground biomass in three biomes. *Global*
632 *Ecology & Biogeography*, 11, 393–399.
- 633 Li, X., & Strahler, A. H. (1985). Geometric-optical modelling of a conifer forest canopy.
634 *IEEE Transactions on Geoscience and Remote Sensing*, GE-23, 705–721.
- 635 Li, X., & Strahler, A. H. (1992). Geometrical-optical bidirectional reflectance modelling
636 of the discrete-crown vegetation canopy: Effect of crown shape and mutual
637 shadowing. *IEEE Transactions on Geoscience and Remote Sensing*, GE-30,
638 276–292.
- 639 Liang, S. (2007). Recent developments in estimating land surface biogeophysical
640 variables from optical remote sensing. *Progress in Physical Geography*, 31,
641 501–516.
- 642 Lim, K., Treitz, P., Baldwin, K., Morrison, I., & Green, J. (2003). Lidar remote sensing
643 of biophysical properties of tolerant northern hardwood forests. *Canadian Journal*
644 *of Remote Sensing*, 29, 658–678.
- 645 McGaughey, R. J. (2010). *FUSION/LDV: Software for LIDAR data analysis and*
646 *Visualization*. Available online (accessed February 24, 2012):
647 <http://forsys.cfr.washington.edu/fusion/fusionlatest.html>.
- 648 McInerney, D. O., Suarez-Minguez, J., Valbuena, R., & Nieuwenhuis, M. (2010). Forest
649 canopy height retrieval using LiDAR data, medium-resolution satellite imagery and
650 kNN estimation in Aberfoyle, Scotland. *Forestry*, 83, 195–206.
- 651 Mora, B., Wulder, M. A., & White, J. C. (2010). Segment-constrained regression tree
652 estimation of forest stand height from very high spatial resolution panchromatic
653 imagery over a boreal environment. *Remote Sensing of Environment*, 114, 2474–
654 2484.
- 655 Næsset, E. & Okland, T. (2002). Estimating tree height and tree crown properties using
656 airborne scanning laser in a boreal nature reserve. *Remote Sensing of Environment*,
657 79, 105–115.
- 658 Natural Resources Canada (2012). *Carbon budget model*. Available online (accessed
659 February 24, 2012): <http://cfs.nrcan.gc.ca/pages/94>.
- 660 Ni-Meister, W., Lee, S., Strahler, A.H., Woodcock, C.E., Schaaf, C., Yao, T., Ranson,
661 K.J., Sun, G., & Blair, J.B. (2010). Assessing general relationships between
662 aboveground biomass and vegetation structure parameters for improved carbon
663 estimate from lidar remote sensing. *Journal of Geophysical Research*, 115,
664 G00E11.
- 665 Pan, Y., Birdsey, R. A., Fang, J., Houghton, R., Kauppi, P. E., Kurz, W. A., Phillips, O.
666 L., Shvidenko, A., Lewis, S. L., Canadell, J. G., Ciais, P., Jackson, R. B., Pacala, S.,

667 McGuire, A. D., Piao, S., Rautiainen, A., Sitch, S., & Hayes, D. (2011). A Large
668 and Persistent Carbon Sink in the World's Forests. *Science*, 333, 988–993.

669 Peddle, D.R., Franklin, S.E., Johnson, R.L., Lavigne, M.B., & Wulder, M.A. (2003).
670 Structural change detection in a disturbed conifer forest using a geometric optical
671 reflectance model in multiple-forward mode. *IEEE Transactions on Geoscience and
672 Remote Sensing*, 41, 163–166.

673 Peddle, D.R., Hall, F.G., & LeDrew, E.F. (1999). Spectral mixture analysis and
674 geometric optical reflectance modeling of boreal forest biophysical structure.
675 *Remote Sensing of Environment*, 67, 288–297.

676 Popescu, S.C., Wynne, R.H., & Nelson, R.H. (2002). Estimating plot-level tree heights
677 with lidar: local filtering with a canopy-height based variable window size.
678 *Computers and Electronics in Agriculture*, 37, 71–95.

679 Potapov, P., Yaroshenko, A., Turubanova, S., Dubinin, M., Laestadius, L., Thies, C.,
680 Aksenov, D., Egorov, A., Yesipova, Y., Glushkov, I., Karpachevskiy, M.,
681 Kostikova, A., Manisha, A., Tsybikova, E., & Zhuravleva, I. (2008). Mapping the
682 world's intact forest landscapes by remote sensing. *Ecology and Society*, 13, 51.

683 Potapov, P., Turubanova, S., & Hansen, M.C. (2011). Regional-scale boreal forest cover
684 and change mapping using Landsat data composites for European Russia. *Remote
685 Sensing of Environment*, 115, 548–516.

686 Rashed, T., Weeks, J. R., Roberts, D. A., Rogan, J., & Powell, R. L. (2003). Measuring
687 the physical composition of urban morphology using multiple endmember spectral
688 mixture models. *Photogrammetric Engineering and Remote Sensing*, 69,
689 1011–1020.

690 Richards, J.A. (1999). *Remote Sensing Digital Image Analysis*, Springer-Verlag, Berlin,
691 p. 240.

692 Somers, B., Asner, G.P., Tits, L., & Coppin, P. (2011). Endmember variability in Spectral
693 Mixture Analysis: A review. *Remote Sensing of Environment*, 115, 1603–1616.

694 Stehman, S. V. (2009). Model-Assisted Estimation as a Unifying Framework for
695 Estimating the Area of Land Cover and Land-Cover Change from Remote Sensing.
696 *Remote Sensing of Environment*, 113, 2455–2462.

697 Stocks, B.J., Mason, J.A., Todd, J.B., Bosch, E.M., Wotton, B.M., Amiro, B.D.,
698 Flannigan, M.D., Hirsch, K.G., Logan, K.A., Martell, D.L., Skinner, W.R. (2003).
699 Large forest fires in Canada, 1959–1997. *Journal of Geophysical Research*, 107,
700 8149, doi:10.1029/2001JD000484.

701 Stojanova, D., Panov, P., Gjorgjioski, V., Kobler, A., & Dzeroski, S. (2010). Estimating
702 vegetation height and canopy cover from remotely sensed data with machine
703 learning. *Ecological Informatics*, 5, 256–266.

704 Tompkins, S., Mustard, J. F., Pieters, C. M., & Forsyth, D. W. (1997). Optimization of
705 endmembers for spectral mixture analysis. *Remote Sensing of Environment*, 59,
706 472–489.

707 Verstraete, M.M., Pinty, B., & Myneni, R.B. (1996). Potential and limitations of
708 information extraction on the terrestrial biosphere from satellite remote sensing.
709 *Remote Sensing of Environment*, 58, 201–214.

710 Woodcock, C., Collins, J., Gopal, A., Jakabhazy, V., Li, X., Macomber, S., Ryherd, S.,
711 Wu, Y., Harward, V., Levitan, J., & Warbington, R. (1994). Mapping forest

712 vegetation using Landsat TM imagery and a canopy reflectance model. *Remote*
713 *Sensing of Environment*, 50, 240–254.

714 Woodcock, C., Collins, J., Jakabhazy, V., Li, X., Macomber, S., & Wu, Y. (1997).
715 Inversion of the Li-Strahler canopy reflectance model for mapping forest structure.
716 *IEEE Transactions on Geoscience and Remote Sensing*, 35, 405–414.

717 Wulder, M.A., & Seemann, D. (2003). Forest inventory height update through the inte-
718 gration of LIDAR data with segmented Landsat imagery. *Canadian Journal of*
719 *Remote Sensing*, 29, 536–543.

720 Wulder, M. A., Campbell, C., White, J. C., Flannigan, M., & Campbell, I. D. (2007).
721 National Circumstances in the International Circumboreal Community. *The*
722 *Forestry Chronicle*, 83, 539–556.

723 Wulder, M. A., Bater C. W., Coops, N. C., Hilker, T., & White, J. C. (2008a). The role of
724 LiDAR in sustainable forest management. *The Forestry Chronicle*, 84, 807–826.

725 Wulder, M.A., White, J.C., Cranny, M., Hall, R.J., Luther, J.E., Beaudoin, A.,
726 Goodenough, D.G., & Dechka, J.A. (2008b). Monitoring Canada’s forests. Part 1 :
727 Completion of the EOSD land cover project. *Canadian Journal of Remote Sensing*,
728 34, 549–562.

729 Wulder, M.A., White, J.C., Masek, J.G., Dwyer, J., & Roy, D.P. (2011). Continuity of
730 Landsat observations: Short term considerations. *Remote Sensing of Environment*,
731 115, 747–751.

732 Wulder, M.A., White, J.C., Nelson, R.F., Næsset, E., Ørka, H.O., Coops, N.C., Hilker, T.,
733 Bater, C.W., & Gobakken, T. (2012). Lidar sampling for large-area forest
734 characterization: A review. *Remote Sensing of Environment*. DOI:
735 <http://dx.doi.org/10.1016/j.rse.2012.02.001>.

736 Zeng, Y., Schaepman, M.E., Wu, B., Clevers, J., & Bregt, A. (2008). Scaling-based forest
737 structural change detection using an inverted geometric-optical model in the Three
738 Gorges region of China. *Remote Sensing of Environment*, 112, 4261–4271.

739 Zhao, K., Popescu, S.C., Meng, X., Pang, Y., & Agca, M. (2011). Characterizing forest
740 canopy structure with lidar composite metrics and machine learning. *Remote*
741 *Sensing of Environment*, 115, 1978–1996.

742 **Tables:**

743

744 **Table 1**

745 Summary statistics for estimates of mean, dominant, and Lorey's height in 81,045 forested
746 lidar plots.

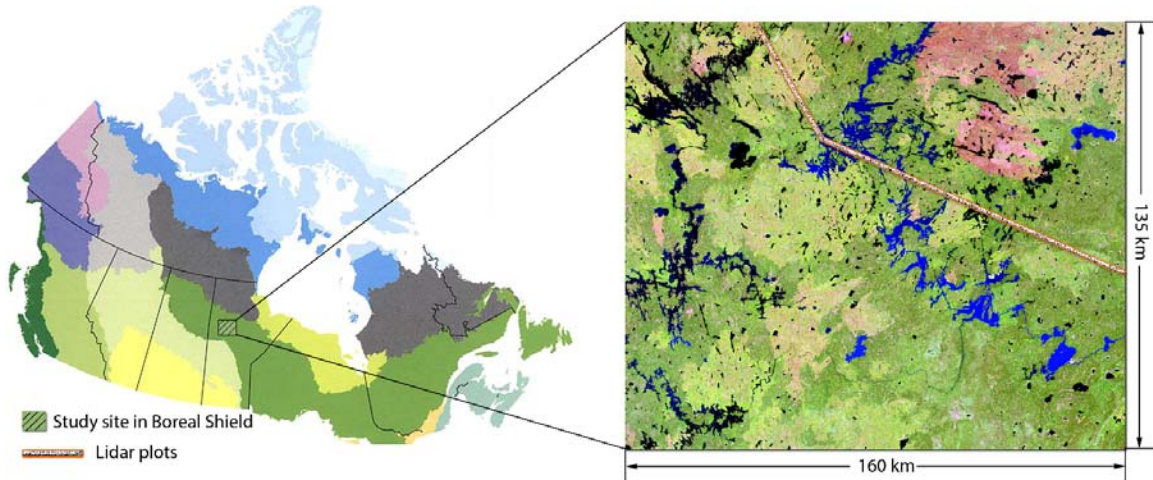
Tree height type	Minimum (m)	Maximum (m)	Mean (m)	Median (m)	Standard deviation (m)
Mean height	5.3	18.5	10.2	10.0	2.1
Dominant height	3.4	27.2	12.5	12.2	4.1
Lorey's height	3.6	23.6	10.3	10.0	3.1

747

748 **Figures:**

749

750

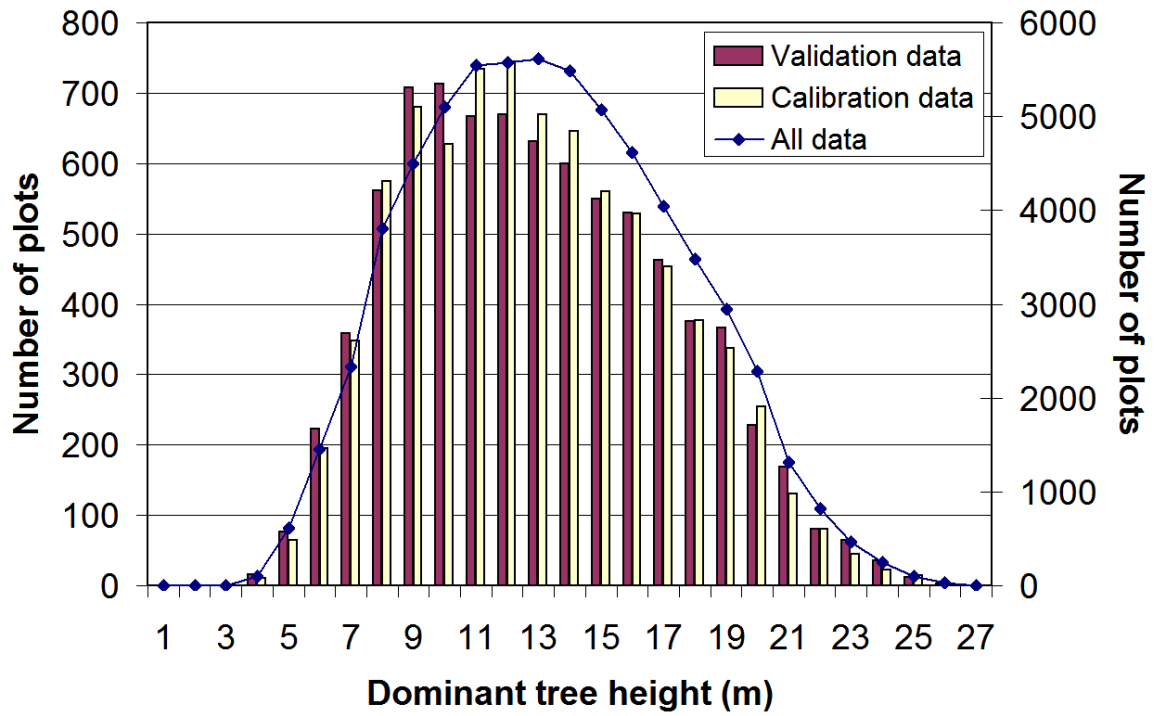


751

752

753 Figure 1. Study area (left) located in western Manitoba, a part of the Boreal Shield ecozone of
754 Canada. The Landsat image (right) is from a color composite using shortwave-infrared,
755 near-infrared, and red bands, and is partially covered by lidar plots (0.27% coverage).

756

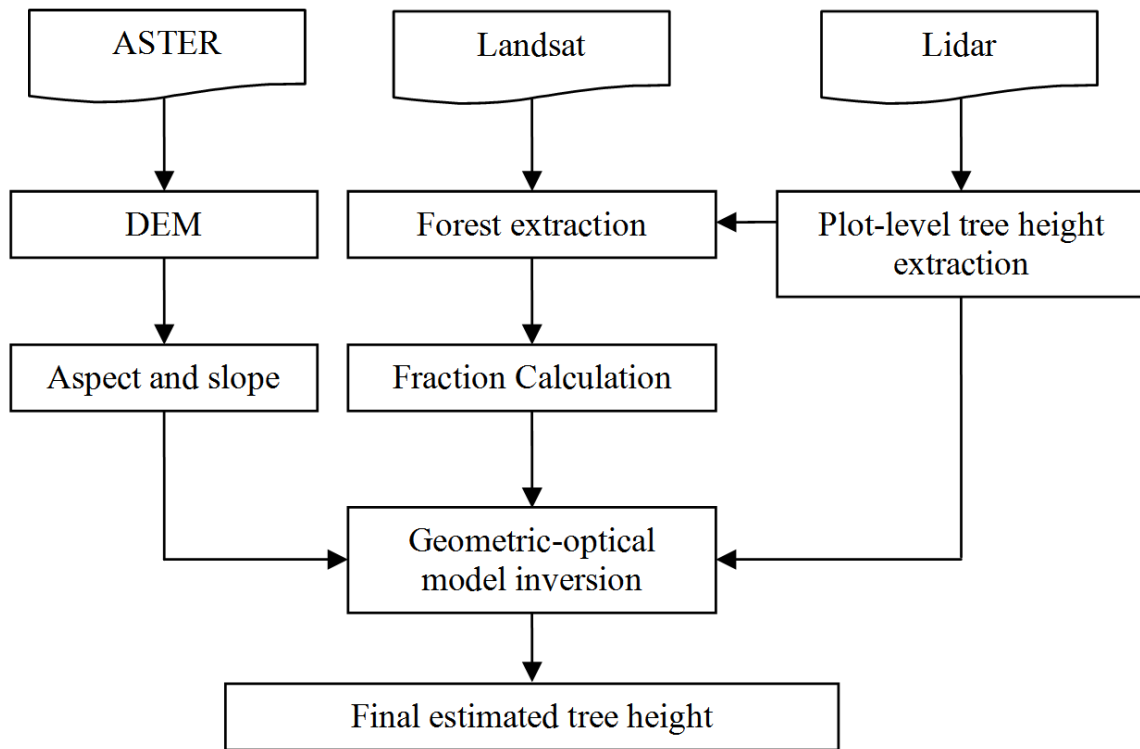


757

758

759 Figure 2. Comparison of three dominant tree height histograms derived from all lidar data, and
760 randomly selected calibration and validation data.

761
762

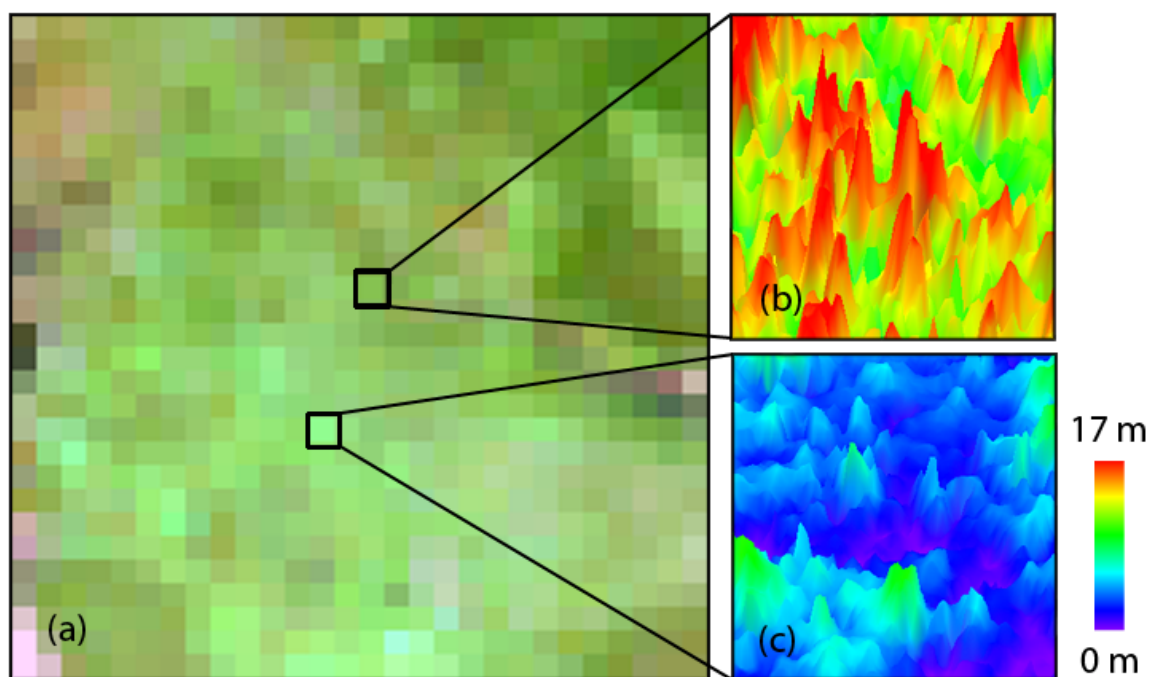


763
764
765
766
767
768
769

Figure 3. A flowchart of the overall approach for estimating tree height using remote sensing data and a geometric-optical model.

770

771



772

773

774 Figure 4. An example of using lidar CHM (canopy height model) in 3D view to

775 distinguish (a) two Landsat pixels representing regions dominated by (b) trees and

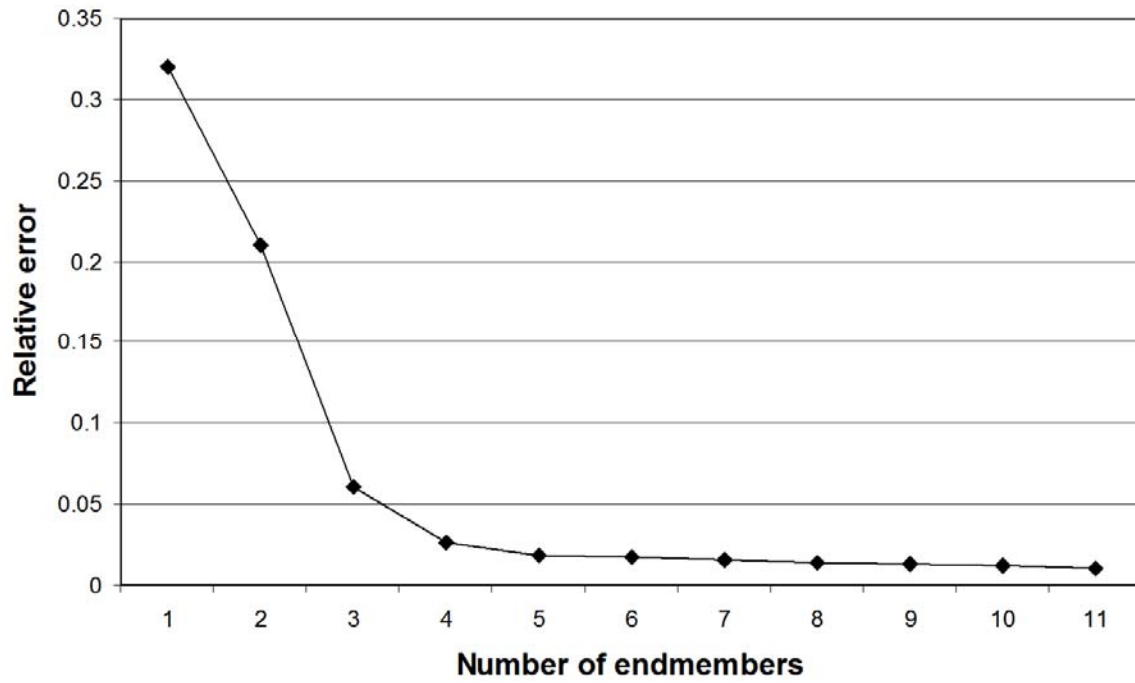
776 (c) low vegetation.

777

778

779

780



781

782

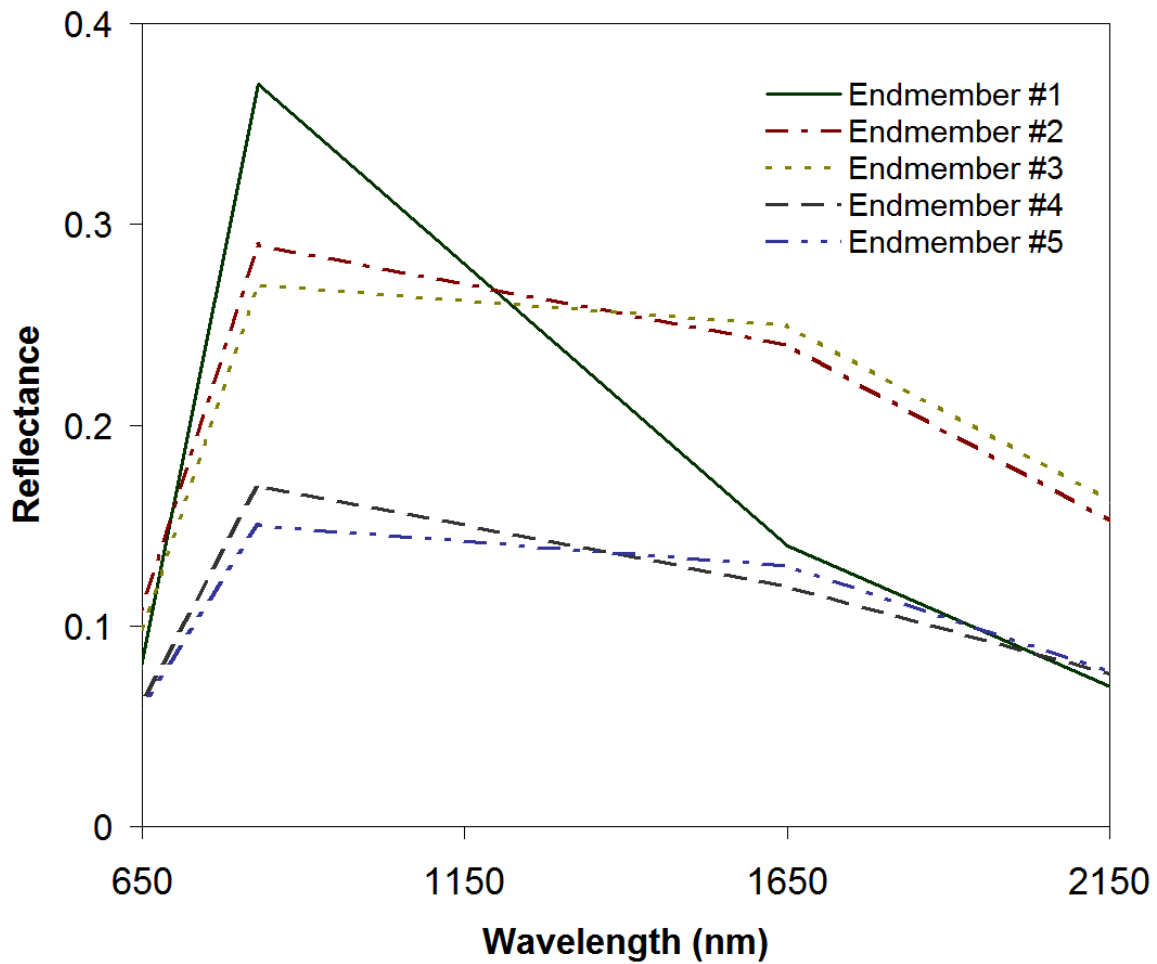
783 Figure 5. SMACC model relative errors calculated using different numbers of
784 endmembers.

785

786

787

788



789

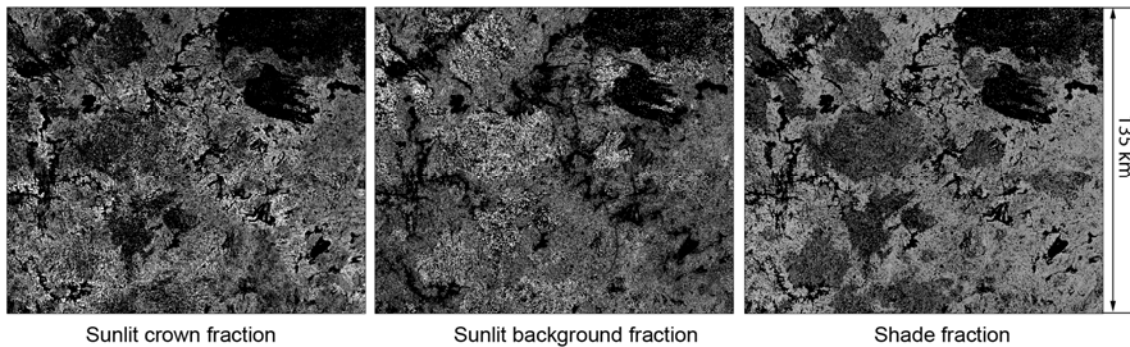
790 Figure 6. Endmember spectra derived from Landsat shortwave-infrared, near-infrared and
791 red bands. Endmember #1 belongs to the sunlit crown, endmembers #2 and #3
792 belong to the sunlit background, and endmembers #4 and #5 belong to the shade
793 fraction.

794

795

796

797



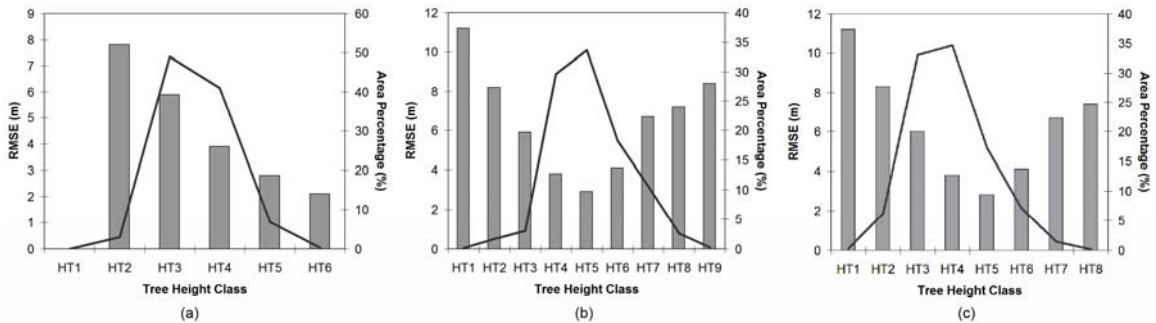
798

799

800 Figure 7. Fraction images of the three forest components of sunlit crown, sunlit
801 background and shade, where grey tones represent values from low (black) to high
802 (bright).

803

804

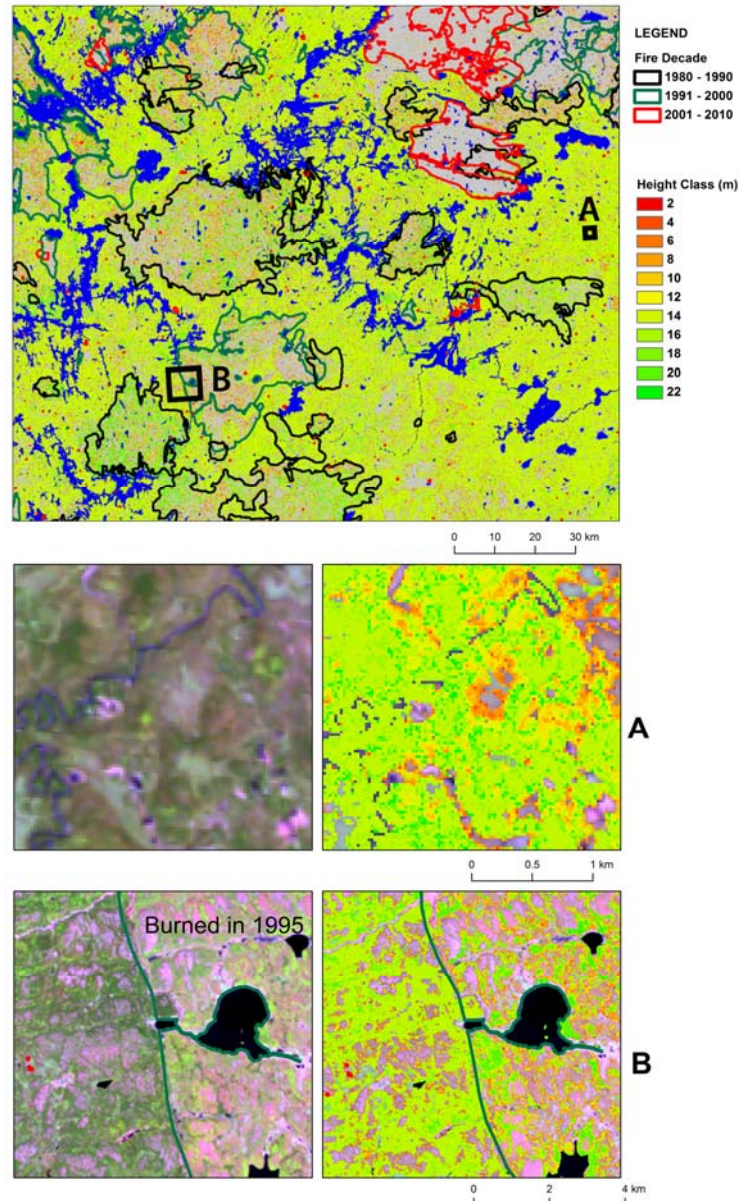


805

806

807 Figure 8. Estimation errors (grey bars) and area percentages (lines) of different tree
808 height classes for (a) mean height, (b) dominant height, and (c) Lorey's height. The
809 height classes (with 3 m interval) are: HT1 (2-5 m), HT2 (5-8 m), HT3 (8-11 m),
810 HT4 (11-14 m), HT5 (14-17 m), HT6 (17-20 m), HT7 (20-23 m), HT8 (23-27 m),
811 and HT9 (27-30 m).

812



814

815 Figure 9. Wall-to-wall estimates of tree height generated from inversion of the Li-Strahler

816 geometric-optical model, overlaid by wildfire boundaries. Insets A and B illustrate

817 the level of detail afforded by the fine-resolution (25 m) forest height estimates.

818 Inset A is a forest and wetland area where variability in height is a function of

819 distance to wetland features. Inset B illustrates variability inside and outside a > 15-

820 year old fire perimeter.

821